The 2018 World Congress on
Advances in Civil, Environmental, & Materials Research (ACEM18)
Songdo Convensia, Incheon, Korea, August 27 - 31, 2018

Seismic analysis between trains and bridges using a localized Lagrange multipliers approach

*Charikleia D. Stoura[1)], Qing Zeng[2)] and Elias G. Dimitrakopoulos[3)]

[1), 2), 3)] *Department of Civil and Environmental Engineering, Hong Kong University of Science and Technology, Clear Water Bay, Kowloon, Hong Kong*
[3)] *ilias@ust.hk*

ABSTRACT

The present paper proposes a time-integration algorithm to study the dynamic interaction of a high-speed train running over a California high-speed railway bridge under an earthquake excitation. The interaction between the two subsystems relies on a localized Lagrange multipliers approach that leads to the partitioned analysis of the vehicle and the bridge in an accurate and cost-efficient manner. The proposed scheme accounts for rolling contact in the tangential direction, and considers nonlinear wheel-rail profiles to simulate detachment and impact events in the normal direction with a nonsmooth approach. The results reveal the unfavorable effect of the seismically induced vibration of the bridge to the safety of the train. The scheme also demonstrates the sequence of wheel-rail contact states that potentially lead to derailment of the train.

1. INTRODUCTION

The increasing ratio of bridges in High-Speed Railway (HSR) lines in conjunction with the high operational speeds of HSR trains (Yang 2004), stresses the importance of accurate and detailed studies on the dynamic vehicle-bridge-interaction (VBI). Especially in the case of an earthquake excitation, the intense seismic response of the interacting vehicle-bridge system (SVBI) may threaten the running safety of trains. Evidently, on October 23, 2004 the Niigata-Chuestu earthquake that hit Japan with a magnitude of 6.8, resulted into the derailment of a Shinkansen train running at 200 km/h. On March 4, 2010, a HSR train derailed due to the Jiashian earthquake in Taiwan (magnitude 6.4), while running at 298 km/h. Finally, Kumamoto earthquake that stroke Japan on April 14, 2016 resulted into the derailment of a Shinkansen bullet train (Zeng 2018a). The aforementioned incidents indicate that even moderate earthquakes can endanger the stability of HSR trains, which create the incentive to reconsider the

---

[1)] Ph.D. Student
[2)] Post-doctoral Fellow
[3)] Associate Professor

dynamics of SVBI systems.

Traditionally, earthquake engineering focuses on the bridge dynamics without the consideration of the interaction with the moving vehicles, which are merely considered as additional masses. The introduction of SVBI shifted the interest from the seismic analysis of the bridge or the vehicle separately, to the joined analysis of the two subsystems. Yang (2002) examined the stability of stationary and moving vehicles on bridges during seismic excitations, and concluded that stationary trains are safer than moving ones. Kim (2006) studied the effect of trains on steel monorail bridges, but focused more on the response of the bridge, revealing the favorable damping effect of the dynamic vehicles on the bridges. Zeng (2016a) investigated the seismic response of coupled vehicle-bridge systems in curved paths and verified the finding of Kim (2006), that the conventional seismic analysis of bridges with the vehicles as additional masses, overestimates the response of bridges. For the evaluation of the running safety of vehicles under earthquakes, most studies adopt force-based metrics, such as the derailment and offload factor (Zeng 2016a, Yang 2002), or geometric criteria, such as the vertical and the lateral wheel-rail displacement (Nishimura 2009). Some recent studies by Ju (2016) and Zeng (2018a) though, assessed more realistically the seismic safety of vehicles, by modelling directly different wheel-rail contact states.

The present study solves the SVBI problem by adopting a localized Lagrange multipliers approach (*partitioned algorithm*), proposed by Zeng (2018b). This method introduces auxiliary contact points to partition the vehicle and the bridge into two subsystems. With the aid of the auxiliary contact points, it assigns two sets of kinematic constraints and subsequently two sets of Lagrange multipliers. This approach is proven to be both accurate and computationally efficient. Motivated by the growing need to simulate realistically the detachment and the derailment of trains running over bridges during earthquakes (Zeng 2018a), the present study extends the numerical analysis scheme of Zeng (2018b) in the following ways: (i) it accounts for rolling contact between the rails and the wheels in the tangential direction, (ii) it considers non-linear profiles for the wheels and the rails, (iii) it accounts for seismic ground motion excitations on the VBI system and (iv) finally it captures realistically different wheel-rail contact states, such as flange contact, wheel climbing up, wheel rail detachment and derailment, according to the linear complementary approach of Zeng (2018a). Finally, the study examines the dynamic interaction of a HSR train and a California HSR bridge consisting of three continuous bridges under an earthquake excitation.

2. PROPOSED VEHICLE-BRIDGE-INTERACTION MODEL

In general, the analysis of the VBI problem can be broken down to three main tasks: (i) the bridge modeling; (ii) the simulation of the vehicles; and (iii) the treatment of the interaction forces. Sections (2.1) to (2.3) discuss the three tasks one by one.

2.1 Bridge model

The bridge model used in this study originates from a California high-speed rail bridge system (Li 2016). The linear elastic bridge system consists of three continuous bridges, each of which comprises of three spans with a uniform length of 33.5m (Fig.

1(a)). Thus, the total length of each continuous bridge is 100.50m, and the whole bridge system is 301.50m long. Each frame comprises three spans according to Fig. 1. The

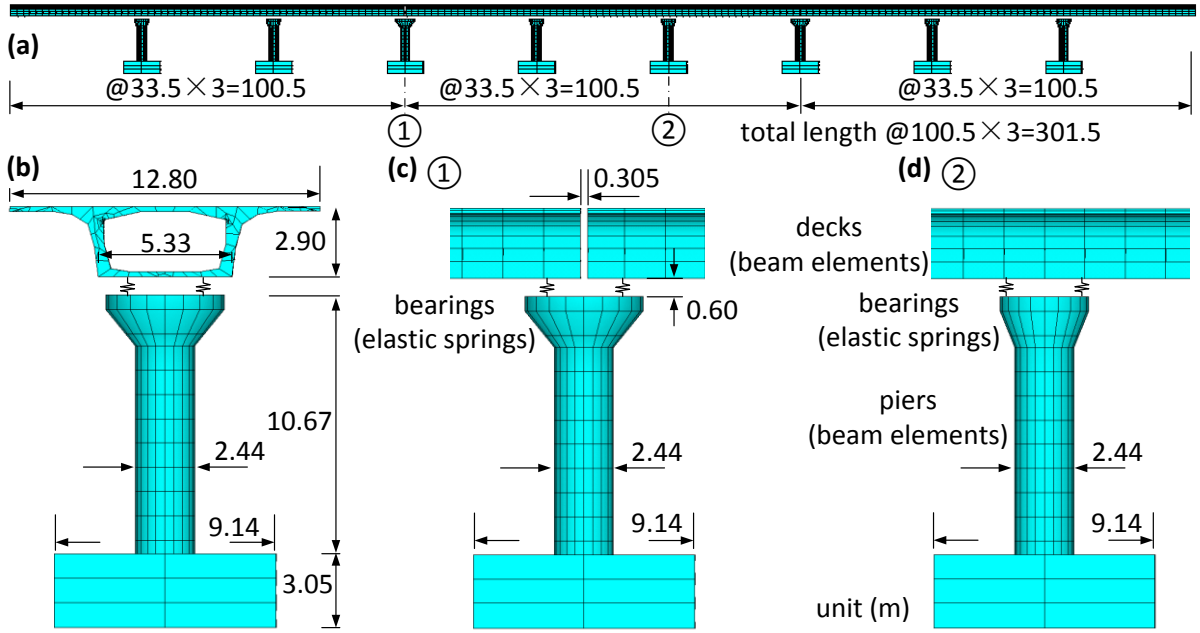

Fig. 1 The considered California high-speed railway bridge system: (a) configuration, (b) back view, (c) section ① and (d) section ② of the bridge.

bridge deck is a single-cell box girder: 12.80m wide at the top, 5.33m wide at the bottom and 2.90m high. Eight single-column piers and two abutments support the post-tensioned deck. All piers are circular with a diameter of 2.44m each and a uniform height of 10.67m. Linear spring elements represent the bearings that connect the bridge deck with the piers and the abutments. The bearings yield in the transverse direction due to the seismic excitation, therefore the post-yield stiffness (Li 2016) rather than the initial stiffness is considered as the effective stiffness.

For the simulation of the bridge, this study employs the Finite Element Method (FEM). Specifically, the mass matrix $\mathbf{M}^B$ and the stiffness matrix $\mathbf{K}^B$ of the bridge are exported with a platform verified in Zeng (2016a). The superscript $(\ )^B$ denotes the bridge subsystem. The damping matrix $\mathbf{C}^B$ is a Rayleigh damping matrix, which is formulated considering the damping ratio of the first two modes of the bridge as 0.05 for seismic analysis (Yang 2004). During the seismic analysis, the reduced flexural stiffness of the piers and the reduced torsional stiffness of the deck, due to the cracking of the concrete section, are taken as half of the uncracked stiffness (Zeng 2016a). The equation of motion (EOM) of the bridge about its static equilibrium position (under its self-weight) is:

$$\mathbf{K}_{\text{eff}}{}^{B}\mathbf{u}^{B}+\mathbf{W}_{N}{}^{B}\boldsymbol{\lambda}_{N}{}^{B}+\mathbf{W}_{T}{}^{B}\boldsymbol{\lambda}_{T}{}^{B}=\mathbf{F}^{B} \tag{1}$$

where $\mathbf{K}_{\text{eff}}{}^{B}$ is the effective stiffness matrix of the bridge system:

$$\mathbf{K}_{\text{eff}}{}^{B}=\mathbf{M}^{B}\frac{d^{2}}{dt^{2}}+\mathbf{C}^{B}\frac{d}{dt}+\mathbf{K}^{B} \tag{2}$$

$\mathbf{u}_{\text{eff}}{}^{B}$ is the displacement vector of the bridge and $\frac{d}{dt}$ denotes time-differentiation. The vector $\mathbf{F}^{B}=-\mathbf{M}^{B}\boldsymbol{\delta}^{B}\ddot{\mathbf{r}}_{OO^{G}}$ contains the seismic forces acting on the bridge, in which $\boldsymbol{\delta}^{B}$ is an influence vector that connects the ground acceleration $\ddot{\mathbf{r}}_{OO^{G}}$ with the pertinent degrees of freedom (DOFs) of the bridge. $\boldsymbol{\lambda}_{N}{}^{B}$ and $\boldsymbol{\lambda}_{T}{}^{B}$ are the normal and the (tangential) creep force vectors, which are discussed later on in Section 2.3. Throughout the study, the subscript $(\ )_{N}$ denotes the normal direction and the subscript $(\ )_{T}$ the tangential direction. $\mathbf{W}_{N}{}^{B}$ and $\mathbf{W}_{T}{}^{B}$ are the contact direction matrices, which include the shape functions of the pertinent DOFs of the bridge. The contact direction matrices of the bridge change with the location of the vehicle, i.e. they are time-dependent.

2.2 Vehicle model

The vehicle model is a three-dimensional (3D) multibody assembly consisting of seven rigid bodies (Dimitrakopoulos 2015, Zeng 2016a, Zeng 2016b): one car body, two bogies and four wheelsets. Linear springs and viscous dashpots connect the distinct components constituting the suspension system of the vehicle. The car body and the bogies have 5 DOFs each, while each wheelset has 4 DOFs according to Fig. 2. The total number of DOFs is 31. The EOM of the vehicle is:

$$\mathbf{K}_{\text{eff}}{}^{V}\mathbf{u}^{V}-\mathbf{W}_{N}{}^{V}\boldsymbol{\lambda}_{N}{}^{V}-\mathbf{W}_{T}{}^{V}\boldsymbol{\lambda}_{T}{}^{V}=\mathbf{F}^{V} \tag{3}$$

where $\mathbf{K}_{\text{eff}}{}^{V}$ is the effective stiffness matrix of the vehicle system:

$$\mathbf{K}_{\text{eff}}{}^{V}=\mathbf{M}^{V}\frac{d^{2}}{dt^{2}}+\mathbf{C}^{V}\frac{d}{dt}+\mathbf{K}^{V} \tag{4}$$

$\mathbf{M}^{V}$, $\mathbf{K}^{V}$ and $\mathbf{C}^{V}$ are the mass, stiffness and damping matrices of the vehicle. $\mathbf{u}^{V}$ is the displacement vector and $\mathbf{F}^{V}=\mathbf{F}_{g}{}^{V}-\mathbf{M}^{V}\boldsymbol{\delta}^{V}\ddot{\mathbf{r}}_{OO^{G}}$ is the external force vector, including the self-weigh $\mathbf{F}_{g}{}^{V}$ and the seismic loads $-\mathbf{M}^{V}\boldsymbol{\delta}^{V}\ddot{\mathbf{r}}_{OO^{G}}$ of the vehicle. Similar to the bridge, $\boldsymbol{\delta}^{V}$ is an influence vector that connects the ground acceleration $\ddot{\mathbf{r}}_{OO^{G}}$ with the DOFs of the vehicle. Finally, $\mathbf{W}_{N}{}^{V}$ and $\mathbf{W}_{T}{}^{V}$ are the contact direction matrices of the vehicle, pertaining to the normal and the (tangential)

creep force vectors $\boldsymbol{\lambda}_N^V$ and $\boldsymbol{\lambda}_T^V$, respectively. The parameters for the modelling of the vehicle are given in (Antolín 2013).

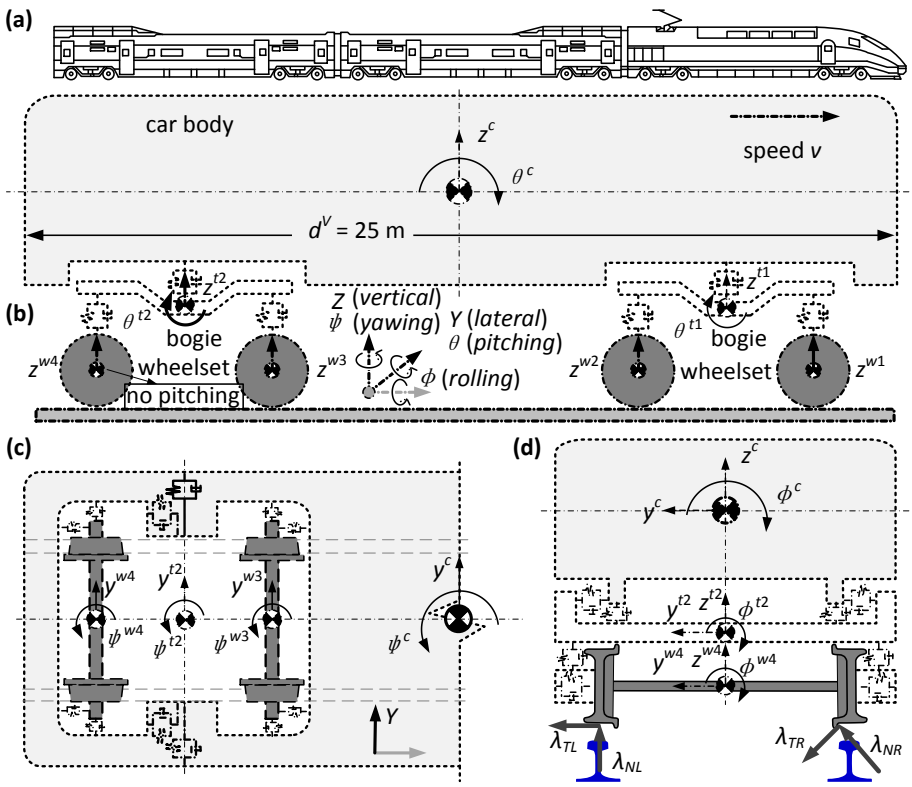

Fig. 2 3D railway vehicle model: (a) a typical HSR train; (b) side view, (c) top view and (d) back view of the vehicle.

2.3 Interaction model – a localized Lagrange multipliers approach

The contact forces between the wheels and the rails couple the vehicle and the bridge subsystems. The rolling contact generates the normal contact force $\boldsymbol{\lambda}_N$ and the creep forces: the longitudinal creep force $\boldsymbol{\lambda}_{Tx}$, the lateral creep force $\boldsymbol{\lambda}_{Ty}$ and the spin moment $\boldsymbol{\lambda}_{Mz}$ (Fig. 3(a)). The normal contact model follows a nonsmooth approach solved as a linear complementarity problem (LCP), proposed by Zeng (2018a). The calculation of the creep forces follows the Kalker's creep model (Kalker 1990) with the nonlinear Shen–Hedrick–Euristic modification (Shen 1983) for high creepage.

A distinct characteristic of the proposed approach is that it introduces artificial auxiliary contact points between the wheels and the rails (Fig. 3(a)). These auxiliary points allow the definition of two sets of kinematic constraints, two sets of normal

contact forces, $\boldsymbol{\lambda}_N{}^V$ and $\boldsymbol{\lambda}_N{}^B$, and two sets of creep contact forces, $\boldsymbol{\lambda}_T{}^V$ and $\boldsymbol{\lambda}_T{}^B$, assigned to the vehicle module and the bridge module, respectively.

2.3.1 Normal contact model

In the normal direction the contact can be either closed or open (Zeng 2018a). In case of closed contact, the contact distance between the rail and the wheel in the normal direction is zero $\mathbf{g}_N = \mathbf{0}$. That indicates wheel-rail impact of instantaneous d u r a t i o n .

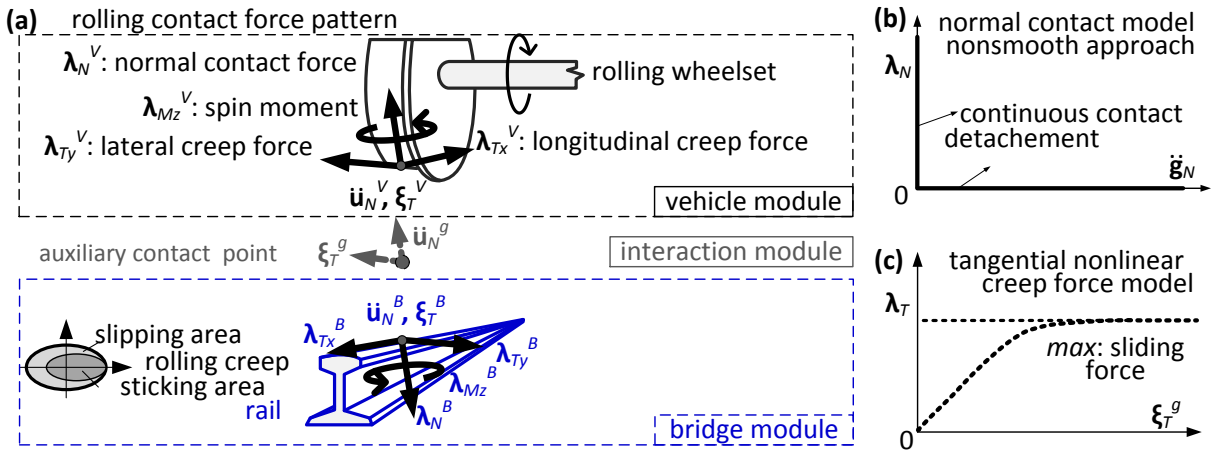

Fig. 3 (a) The 3D wheel–rail rolling contact model according to the partitioned algorithm, (b) the normal contact model and (c) the tangential contact model.

When additionally the contact velocity and acceleration is zero $\dot{\mathbf{g}}_N = \ddot{\mathbf{g}}_N = \mathbf{0}$, there exists continuous contact of finite duration. In case of open contact (detachment), the normal contact force is equal to zero $\boldsymbol{\lambda}_N = \mathbf{0}$. The transition between the two contact states is captured as a LCP with the Signorini conditions (Zeng 2018a) describing *continuous contact* and *detachment* (Fig. 3(b)).

During continuous contact, the interaction model in the normal direction adopts the "rigid contact" assumption. That means that the vehicle wheels and the rails stay in contact and do not deform. Considering $\ddot{\mathbf{u}}_N{}^g$ as the global acceleration of the auxiliary contact point in the normal direction, the kinematic constraints on the acceleration level (continuous contact) are (Zeng 2018b):

$$\begin{cases} \left(\mathbf{W}_{N\,\mathrm{eff}}{}^V\right)^{\mathrm{T}} \mathbf{u}^V + v^2 \mathbf{r}''_{cN} = \mathbf{E}_N{}^V \ddot{\mathbf{u}}_N{}^g \\ \left(\mathbf{W}_{N\,\mathrm{eff}}{}^B\right)^{\mathrm{T}} \mathbf{u}^B = \mathbf{E}_N{}^B \ddot{\mathbf{u}}_N{}^g \end{cases} \tag{5}$$

where $\mathbf{r}_{cN}$ represents the vector of normal rail irregularities. $\mathbf{E}_N{}^V$ and $\mathbf{E}_N{}^B$ are identity matrices pertaining to the vehicle and the bridge. For brevity, the two

abbreviations $\mathbf{W}_{N\mathrm{eff}}{}^{V}$ and $\mathbf{W}_{N\mathrm{eff}}{}^{B}$ represent the effective normal contact direction matrices as follows:

$$\begin{aligned}\left(\mathbf{W}_{N\mathrm{eff}}{}^{V}\right)^{\mathrm{T}} &= \left(\mathbf{W}_{N}{}^{V}\right)^{\mathrm{T}}\frac{d^2}{dt^2},\\ \left(\mathbf{W}_{N\mathrm{eff}}{}^{B}\right)^{\mathrm{T}} &= \left(\mathbf{W}_{N}{}^{B}\right)^{\mathrm{T}}\frac{d^2}{dt^2}+2v\left(\mathbf{W}_{N}'{}^{B}\right)^{\mathrm{T}}\frac{d}{dt}+v^2\left(\mathbf{W}_{N}''{}^{B}\right)^{\mathrm{T}}\end{aligned} \tag{6}$$

The normal impact follows Newton's impact law on the velocity level (Zeng 2018a), with the coefficient of restitution considered as $\varepsilon_N = 0$.

2.3.2 Tangential contact model

The creep forces are expressed as the product of the saturation constant $\boldsymbol{\varepsilon}$ (Shen 1983), the Kalker's creep coefficient matrix $\mathbf{f}_T$ and the creepage $\boldsymbol{\xi}_T{}^{g}$ (Kalker 1990).

$$\begin{cases}\mathbf{E}_T{}^{V}\boldsymbol{\lambda}_T{}^{V} = \boldsymbol{\varepsilon}\mathbf{f}_T\boldsymbol{\xi}_T{}^{V}\\ \mathbf{E}_T{}^{B}\boldsymbol{\lambda}_T{}^{B} = \boldsymbol{\varepsilon}\mathbf{f}_T\boldsymbol{\xi}_T{}^{B}\end{cases} \tag{7}$$

where $\mathbf{E}_T{}^{V}$ and $\mathbf{E}_T{}^{B}$ are identity matrices pertaining to the vehicle and the bridge and $\boldsymbol{\xi}_T{}^{V} = \boldsymbol{\xi}_T{}^{B} = \boldsymbol{\xi}_T{}^{g}$ denotes the creepage (the relative wheel-rail velocity in the tangential direction normalized by the vehicle speed v) pertaining to the vehicle and the bridge (Zeng 2016a). Similar to the normal direction, the two abbreviations $\mathbf{W}_{T\mathrm{eff}}{}^{V}$ and $\mathbf{W}_{T\mathrm{eff}}{}^{B}$ represent the effective tangential contact direction matrices:

$$\begin{aligned}\mathbf{W}_{T\mathrm{eff}}{}^{V} &= \left(\mathbf{W}_{T}{}^{V}\right)\frac{d}{dt},\\ \mathbf{W}_{T\mathrm{eff}}{}^{B} &= \left(\left(\mathbf{W}_{T}{}^{B}\right)\frac{d}{dt}+v\left(\mathbf{W}_{T}'{}^{B}\right)\right)\end{aligned} \tag{8}$$

2.3.3 Solution of the EOMs and integration scheme

Following Newton's third law, the two sets of contact forces (Lagrange multipliers and creep forces) are connected (Fig. 3(a)) as:

$$\begin{cases}\mathbf{E}_N{}^{V}\boldsymbol{\lambda}_N{}^{V} = \mathbf{E}_N{}^{B}\boldsymbol{\lambda}_N{}^{B}\\ \mathbf{E}_T{}^{V}\boldsymbol{\lambda}_T{}^{V} = \mathbf{E}_T{}^{B}\boldsymbol{\lambda}_T{}^{B}\end{cases} \tag{9}$$

Gathering the equilibrium and compatibility equations of the system (Eqs. (2), (4), (5), (7), and (9), and the expression of creepage from Zeng (2016a) yields:

$$\begin{aligned}&\mathbf{S}_l\left[\mathbf{u}^V \quad \mathbf{u}^B \quad \boldsymbol{\lambda}_N{}^V \quad \boldsymbol{\lambda}_N{}^B \quad \boldsymbol{\lambda}_T{}^V \quad \boldsymbol{\lambda}_T{}^B \quad \ddot{\mathbf{u}}_N{}^g \quad \boldsymbol{\xi}_T{}^g\right]^{\mathrm{T}}\\ &=\left[\mathbf{F}^V \quad \mathbf{F}^B \quad v^2\mathbf{r}_c'' \quad \mathbf{0} \quad \mathbf{0} \quad \mathbf{0} \quad \mathbf{0} \quad \left(-v\mathbf{r}_{cT}'' - \left(\mathbf{W}_T{}^V\right)\mathbf{b}\dot{\boldsymbol{\theta}}^V\right)\right]^{\mathrm{T}}\end{aligned} \tag{10}$$

where $\mathbf{S}_l$ is the differential operator:

$$\mathbf{S}_l = \begin{bmatrix} \mathbf{K}_{\mathrm{eff}}{}^V & \mathbf{0} & -\mathbf{W}_N{}^V & \mathbf{0} & -\mathbf{A}^{\mathrm{T}}\mathbf{W}_T{}^V & \mathbf{0} & \mathbf{0} & \mathbf{0} \\ \mathbf{0} & \mathbf{K}_{\mathrm{eff}}{}^B & \mathbf{0} & \mathbf{W}_N{}^B & \mathbf{0} & \mathbf{W}_T{}^B & \mathbf{0} & \mathbf{0} \\ \left(-\mathbf{W}_{N\mathrm{eff}}{}^V\right)^{\mathrm{T}} & \mathbf{0} & \mathbf{0} & \mathbf{0} & \mathbf{0} & \mathbf{0} & \mathbf{E}_N{}^V & \mathbf{0} \\ \mathbf{0} & \left(\mathbf{W}_{N\mathrm{eff}}{}^B\right)^{\mathrm{T}} & \mathbf{0} & \mathbf{0} & \mathbf{0} & \mathbf{0} & -\mathbf{E}_N{}^B & \mathbf{0} \\ \mathbf{0} & \mathbf{0} & \left(\mathbf{E}_N{}^V\right)^{\mathrm{T}} & \left(-\mathbf{E}_N{}^B\right)^{\mathrm{T}} & \mathbf{0} & \mathbf{0} & \mathbf{0} & \mathbf{0} \\ \mathbf{0} & \mathbf{0} & \mathbf{0} & \mathbf{0} & \left(\mathbf{E}^V{}_T\right)^{\mathrm{T}} & \mathbf{0} & \mathbf{0} & -\boldsymbol{\varepsilon}\mathbf{f}_T \\ \mathbf{0} & \mathbf{0} & \mathbf{0} & \mathbf{0} & \mathbf{0} & \left(\mathbf{E}_T{}^B\right)^{\mathrm{T}} & \mathbf{0} & -\boldsymbol{\varepsilon}\mathbf{f}_T \\ \left(\mathbf{W}_{T\mathrm{eff}}{}^V\right)^{\mathrm{T}}\mathbf{A} & \left(-\mathbf{W}_{T\mathrm{eff}}{}^B\right)^{\mathrm{T}} & \mathbf{0} & \mathbf{0} & \mathbf{0} & \mathbf{0} & \mathbf{0} & v\left(-\mathbf{E}_T\right)^{\mathrm{T}} \end{bmatrix} \tag{11}$$

where $\mathbf{A}$ is an auxiliary matrix and $\mathbf{b}$ an auxiliary vector to include the additional angular pitching velocity vector $\dot{\boldsymbol{\theta}}^w$ of the wheelsets (excluded in Fig. 2(a)) (Zeng 2016a). The solution of Eq. (10) returns simultaneously the displacements and the contact forces of both the vehicle and the bridge, as well as the boundary accelerations and creepages of the auxiliary contact points.

The first two rows of Eq. (10) are the EOMs of the vehicle (Eq. (3)) and the bridge (Eq. (1)), respectively. The third and the fourth row are the two sets of kinematic constraints on the acceleration level (Eq. (5)). The fifth row is Newton's third law pertaining to the normal contact force (Eq. (9)). The sixth and the seventh row give the tangential creep forces pertaining to the vehicle and the bridge (Eq. (7)). The last (seventh) row gives the formulation of the creepage. The integration of Eq. (10) follows the Newmark-beta method (Newmark 1959) with γ = 1/2 and β = 1/4. Following the same procedure as (Zeng 2018), the expression of the displacement vectors, the contact force vectors, the global acceleration vector and the creepage vector at the next time-step result. The proposed time-integration scheme is realized in MATLAB software (MathWorks 2017).

3. VALIDATIONS AND NUMERICAL EXAMPLES

3.1 A train vehicle over rigid rails

This example concerns a (half) train vehicle running on rigid rails, originally used by Nishimura (2009) to study the derailment of vehicles under track excitations, and later on employed by Zeng (2018a) to verify their approach to capture discontinuous events (impact and detachment). The train vehicle consists of one car body, one bogie

and two wheelsets. Each component has 3 DOFs: one lateral y, one vertical z and one rolling φ. The total number of DOFs of the vehicle is 12. The car body, the bogie and the wheelsets are connected with linear spring and dashpots, the properties of which are given in Nishimura (2009). The track system consists of springs and dampers between the rails and the ground (Nishimura 2009). The vehicle runs on the rail with speed 300km/h, while excited by a five-cycle sine wave with frequency 0.5Hz and amplitude 320mm in the lateral direction. In the tangential direction, the contact force follows the

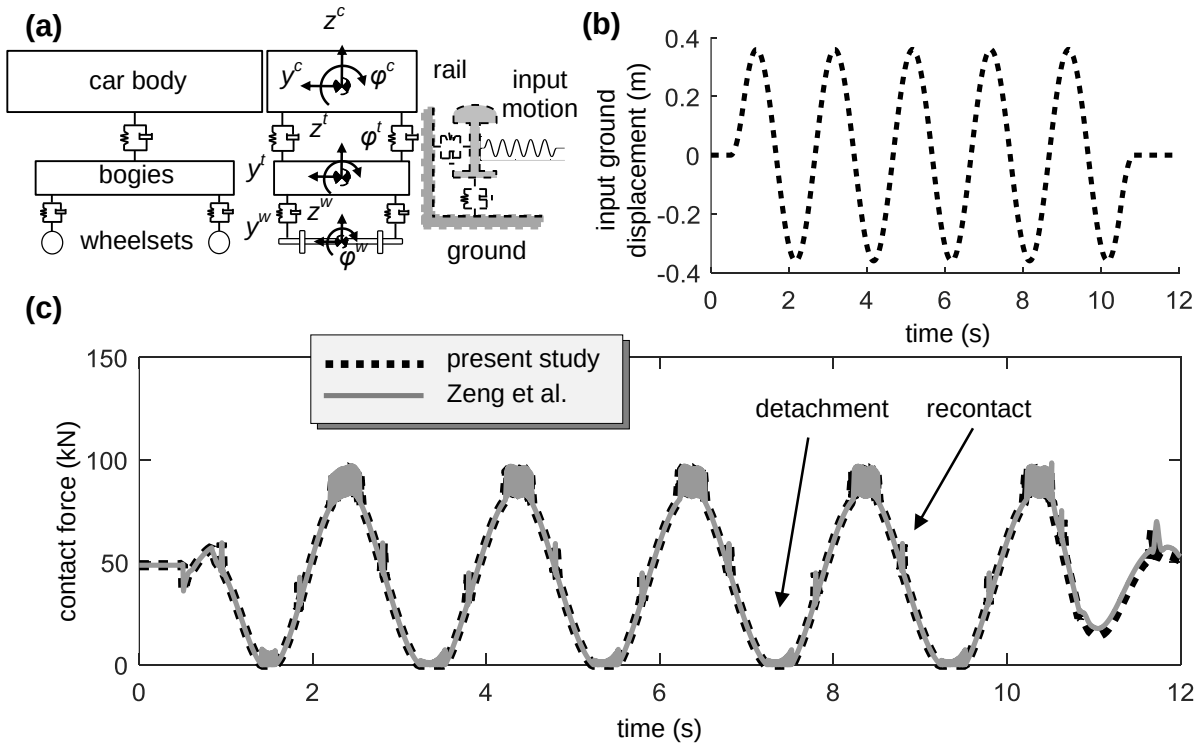

Fig. 4 (a) The 12-DOF half vehicle model, (b) the input lateral ground motion for all three methods and (c) the time-history of the wheel-rail vertical contact force of the right wheel.

Kalker's linear creep theory (Kalker 1990) and the wheel-rail profile is the same as in Zeng (2018a). The study compares the response of the vehicle with the proposed method and the approach of Zeng (2018a). The time step of the analysis is dt = 0.001s and the analysis ends at 12s. The calculations are performed using a computer Intel(R) Core(TM) i5-6600 CPU @ 3.30 GHz.

Fig. 4 plots the 12-DOF half vehicle (Fig. 4(a)), the five-cycle input ground motion (Fig. 4(b)), which is the same for both approaches, and the time-history of the vertical contact force of the right wheel of the vehicle (Fig. 4(c)). Zero contact force in Fig. 4(c) indicates the detachment of the wheel from the rail, while when the contact force obtains again values larger than zero, recontact happens. The response-history of both methods shows a good agreement. However, the proposed partitioned algorithm is more time-efficient compared to that of Zeng (2018a). The time cost of the partitioned

method is 1.37h, while for the coupled approach proposed by Zeng (2018a) the computational time is 5.92h. Evidently, the present approach is 4.3 times faster, suggesting that the proposed partitioned scheme is both accurate and computationally efficient for the solution of complicated VBI problems.

3.2 A two-vehicle train over three HSR continuous bridges

This section tackles a realistic and computationally heavy VBI problem. It examines a train consisting of two identical vehicles (Fig. 2, Section 2.2) running with a constant

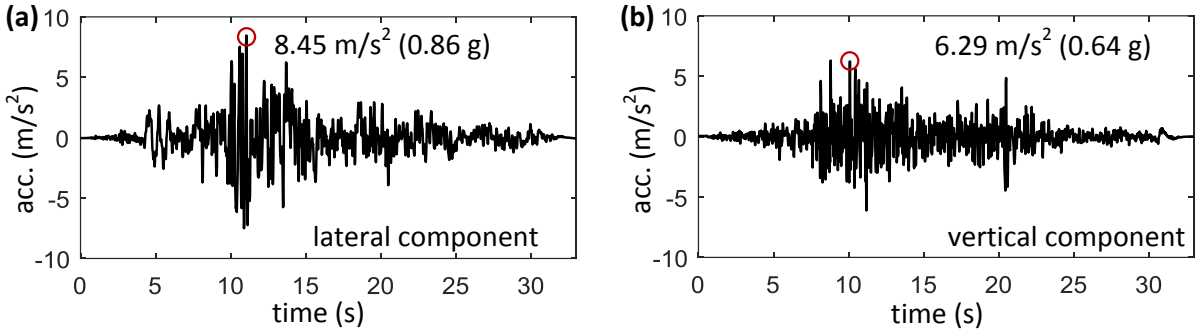

Fig. 5 The acceleration time histories of the ground motion recorded on September 16, 1978 in Tabas Iran, at Tabas station: (a) the lateral component and (b) the vertical component.

speed of 300km/h (83.33m/s) over the continuous bridges system of Li (2016) (Section 2.1) during a strong earthquake. Fig. 5 plots the lateral (Fig. 5(a)) and vertical (Fig. 5(b)) acceleration time histories of the ground motion recorded on September 16, 1978, at Tabas Station in Tabas Iran, 6.96km away from the epicenter of a 7.35 magnitude earthquake event (PEERC database 2015).

The total length of the three continuous bridges system of Fig. 1 is 301.50 m, therefore the 2 • 25m long vehicle (Fig. 2) needs (301.50m + 2 • 25m =) 351.5m / 83.33m/s = 4.218s to pass over the bridge system. The study assumes that the earthquake of Fig. 5 strikes at t = 0s, when the time-history analysis begins. However, in reality, the position of a train vehicle running over a bridge when an earthquake strikes is unpredictable. Therefore, in order to examine an unfavorable scenario, the analysis considers that the 1st vehicle runs on the rigid ground from 0 – 2s and then enters the seismically vibrating bridge system, when the most intense part of the seismic vibration begins (Fig. 5).

Fig. 6 illustrates the response of both the bridge and the vehicle during the ground motion of Fig. 5. It also indicates the position of the train when detachment of the 1st vehicle from the rails happens (t = 4.667s). The analysis terminates at t = 4.703s due to derailment of the 1st vehicle. At that time, the train moves on the 3rd bridge of the continuous bridges system (Fig. 6). According to Fig. 6(b), when only the earthquake acts on the bridge system, each bridge vibrates around its static equilibrium position under its self-weight (0 – 2s). Under the combined effect of the dynamic VBI and the seismic shaking all three bridges defelect downwards. This is more evident for the 1st

(dash-dot blue line) and the 2nd (dot black line) bridge (Fig. 6(b)), as the vehcile enters the 3rd bridge (continuous grey line) just before the derailment. That reveals that when the earthquake excitation is not very intense (0 – 5s in Fig. 5(b)), the moving vehicle rather than the earthquake affects the response of the bridge in the vertical direction. In the lateral direction, the earthquake is the main source of excitation (Fig. 6(a)), since the response of all three bridges becomes larger as the intensity of the earthquake motion increases (Fig. 5(a)).

When the vehicle reaches the 3rd bridge, wheel-rail detachment happens, which eventually leads to derailment of the 1st vehicle. The derailment happens before the

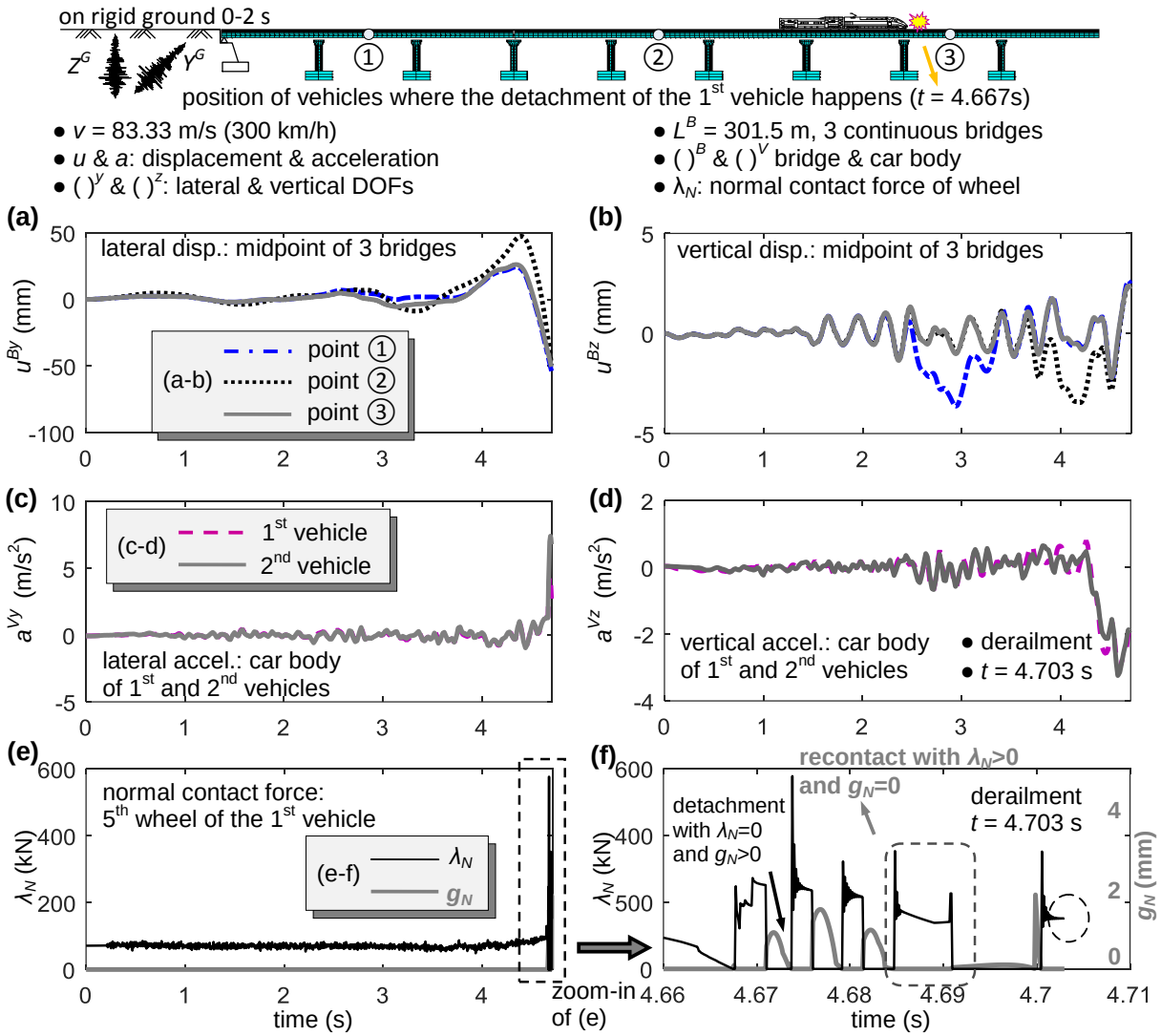

Fig. 6 The response histories of the VBI system under the ground motion of Fig. 5: (a) the lateral and (b) the vertical displacement of the midpoints of the three bridges, (c) the lateral and (d) the vertical acceleration of the car bodies of the two vehicles, (e) the normal contact force of the 5th wheel of the 1st vehicle and (f) the pertinent zoom-in of (e) together with the contact distance of the same wheel.

strong intensity component of the earthquake, indicating that ground motions of even low intensity can jeopardize the stability of vehicles moving on bridges. The results verify the adverse effect of the seismically induced vibration of the bridges to the safety of the vehicles, according to Zeng (2018a). The detachment becomes more evident in Fig. 6(e) that plots the normal contact force of the 5th wheel of the 1st vehicle, as well as in Fig. 6(f) that zooms in the contact force at the time of derailment. When detachment happens at t = 4.667s, the normal contact force λ_N becomes zero, while the contact distance g_N (gray line) is greater than zero. The impact following is characterized by contact

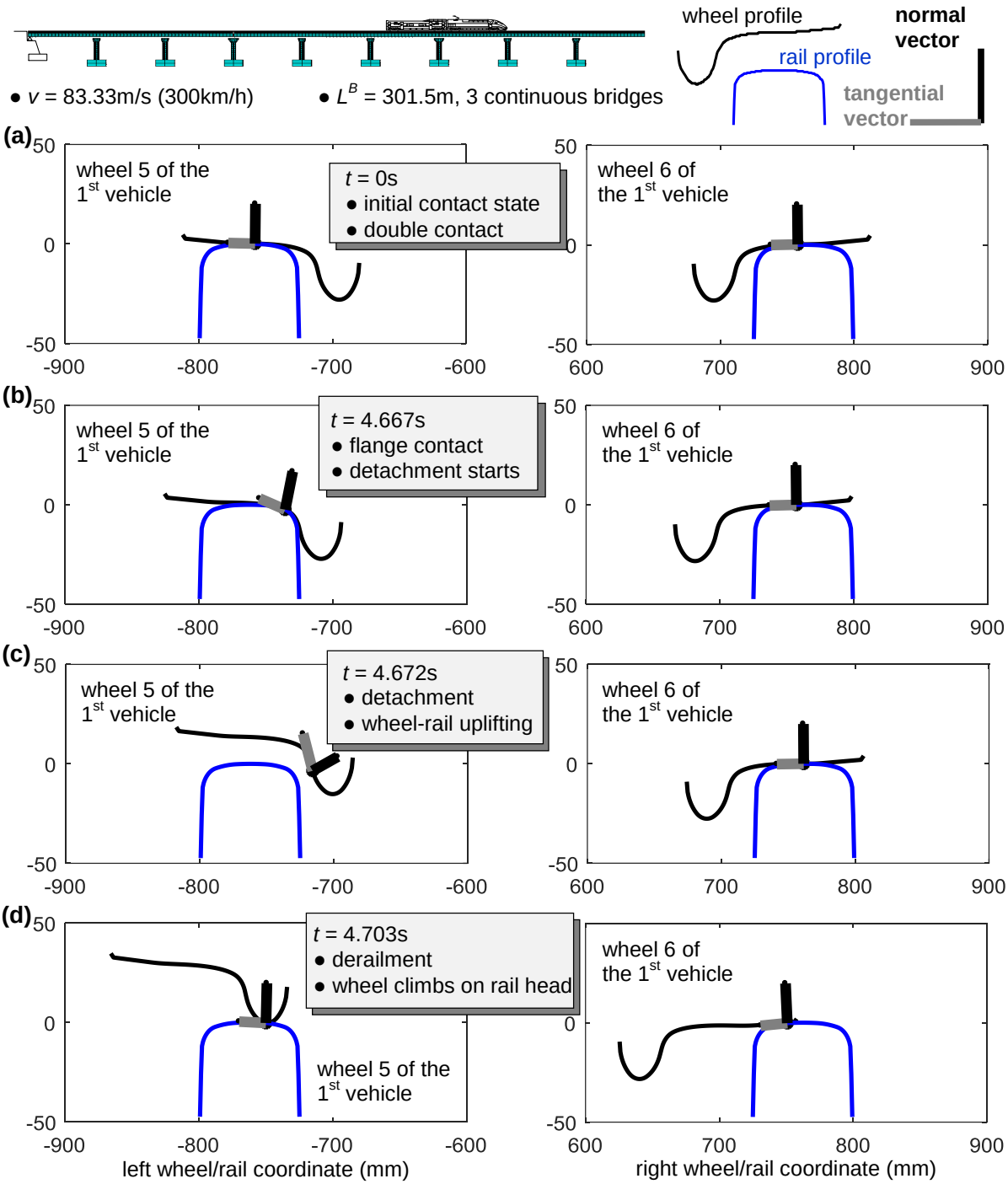

Fig. 7 The wheel-rail kinematics for the 3rd wheelset (wheels 5 and 6) of the 1st vehicle for four different wheel-rail contact states: (a) the initial state (double contact), (b) the flange contact of wheel 5, (c) the detachment of wheel 5 and (d) the derailment of wheel 5 under the ground motion of Fig. 5.

force λ_N larger than zero and g_N equal to zero. After successive detachments and impacts, derailment happens at t = 4.703s.

Finally, according to Figs. 7(c) and (d), the acceleration of the vehicle in both the normal and the lateral direction under the seismic excitation exceeds the riding comfort thresholds of the HSR codes (China's Ministry of Railways 2009). More specifically, the peak vertical acceleration of the car body is larger than 1.28m/s^2 (Fig. 6 (d)) and the peak lateral acceleration is larger than 0.98m/s^2 (Fig. 6 (c)).

To elucidate the different contact states, Fig. 7 illustrates the contact state in case of double contact (Fig. 7(a)), and the sequence of the wheel-rail contact events leading to the derailment of the 3rd wheelset (wheels 5 and 6) of the 1st vehicle (Figs. 7(b), (c) and (d)): at t = 4.667s the detachment of the 5th wheel (of the 3rd wheelset) starts indicated by flange contact (Fig. 7(b)), at t = 4.672s wheel 5 detaches by the rail (Fig. 7(c)) and finally at t = 4.703s the same wheel climbs over the rail head leading to derailment of the wheelset (Fig. 7(d)).

4. CONCLUSIONS

This study presents an accurate and cost-efficient SVBI analysis scheme that models directly different contact states in order to examine the dynamic seismic response of a California HSR bridge under the passage of a HSR train. Therefore, it extends the localized Lagrange multipliers approach, in order to account for creep forces in the tangential direction and seismic excitations. Simultaneously, it employs practical nonlinear wheel-rail profiles in order to simulate realistically different contact states of the coupled vehicle-bridge system such as flange contact, wheel climbing-up over the rail, wheel uplifting and derailment. To verify the accuracy of the proposed scheme, the study first studies a half vehicle running over a track system connected with spring and dashpots to the ground. The results are in good agreement with the existing analysis schemes, and they show that the proposed partitioned algorithm can decrease significantly the time cost of the analysis.

More importantly though, the study examines the realistic scenario of a two-vehicle train running over three continuous HSR bridges under a historic ground motion. The results illustrate the unfavorable effect of the seismic induced vibration of the bridge to the safety of the vehicle. At the same time, the practical wheel-rail profiles adopted herein enable the accurate simulation of the wheel-rail contact states, when examining a coupled vehicle-bridge system during earthquake excitations.

5. ACKNOWLEDGEMENTS

This study was supported by the Research Grants Council of Hong Kong, under Grant Reference Number: 16244116. The first author would also like to acknowledge the Hong Kong PhD Fellowship Scheme 2017/2018 (PF16-07238).

REFERENCES

Antolín, P., Zhang, N., Goicolea, J.M., Xia, H., Astiz, M.Á and Oliva, J. (2013) "Consideration of nonlinear wheel–rail contact forces for dynamic vehicle–bridge interaction in high-speed railways", *J. Sound Vibrat.,* **332**(5), 1231-51.

(2009), *Code for Design of High Speed Railways*.

Dimitrakopoulos, E.G. and Zeng, Q. (2015) "A three-dimensional dynamic analysis scheme for the interaction between trains and curved railway bridges", *Comput. Struct.,* **149**, 43-60.

Ju, S. (2016) "A frictional contact finite element for wheel/rail dynamic simulations", *Nonlinear Dyn.,* **85**(1), 365-74.

Kalker, J.J. (1990) "Variational and Numerical Theory of Contact", Three-Dimensional Elastic Bodies in Rolling Contact Springer, 137-184.

Kim, C. and Kawatani, M. (2006) "Effect of train dynamics on seismic response of steel monorail bridges under moderate ground motion", *Earthquake Eng. Struct. Dyn.,* **35**(10), 1225-45.

Li, Y. and Conte, J.P. (2016) "Effects of seismic isolation on the seismic response of a California high-speed rail prototype bridge with soil-structure and track-structure interactions", *Earthquake Eng. Struct. Dyn.,* **45**(15), 2415-34.

MathWorks (2017), *MATLAB User's Guide,* MA: The MathWorks Inc., Natick, Massachusetts, United States.

Newmark, N.M. (1959) "A method of computation for structural dynamics", *J. Eng. Mech. Div.,* **85**(3), 67-94.

Nishimura, K., Terumichi, Y., Morimura, T. and Sogabe, K. (2009) "Development of vehicle dynamics simulation for safety analyses of rail vehicles on excited tracks", *J. Comput. Nonlinear Dyn.,* **4**(1), 011001.

PEERC database (2015), available at: https://ngawest2.berkeley.edu/site. Accessed May, 2018.

Shen, Z.Y., Hedrick, J.K. and Elkins, J.A. (1983) "A comparison of alternative creep force models for rail vehicle dynamic analysis", *Veh. Syst. Dyn.,* **12**(1-3), 79-83.

Yang, Y.B., Yau, J.D., Yao, Z. and Wu, Y.S. (2004), *Vehicle-bridge interaction dynamics: with applications to high-speed railways,* World Scientific, Singapore.

Yang, Y.B. and Wu, Y.S. (2002) "Dynamic stability of trains moving over bridges shaken by earthquakes", *J. Sound Vibrat.,* **258**(1), 65-94.

Zeng, Q. and Dimitrakopoulos, E.G. (2018a) "Vehicle–bridge interaction analysis modeling derailment during earthquakes", *Nonlinear Dyn.*, 1-23.

Zeng, Q., Stoura, C.D. and Dimitrakopoulos, E.G. (2018b) "A localized lagrange multipliers approach for the problem of vehicle-bridge-interaction", *Eng. Struct.,* **168**, 82-92.

Zeng, Q. and Dimitrakopoulos, E.G. (2016a) "Seismic response analysis of an interacting curved bridge–train system under frequent earthquakes", *Earthquake Eng. Struct. Dyn.,* **45**(7), 1129-48.

Zeng, Q., Yang, Y.B. and Dimitrakopoulos, E.G. (2016b) "Dynamic response of high speed vehicles and sustaining curved bridges under conditions of resonance", *Eng. Struct.,* **114**, 61-74.